A *V*-Band Wafer Probe Using Ridge-Trough Waveguide

Edward M. Godshalk, *Member*, *IEEE*

Abstract—**In this paper a *V*-band (50–75 GHz) wafer probe is presented. The probe features a new type of waveguide developed to allow transition from rectangular waveguide to coplanar waveguide. This new waveguide consists of a ridge extending from the upper waveguide wall into a trough in the lower waveguide wall, and is known as ridge-trough waveguide. A mathematical model is presented that allows the important properties of the ridge-trough waveguide to be calculated such as the cutoff frequency and characteristic impedance.**

I. Introduction

IN FIG. 1 a coplanar waveguide (CPW) probe is shown in a typical wafer probing orientation. The CPW is formed by depositing a layer of gold on the bottom surface of an alumina board forming the structure shown. When the alumina board is placed in contact with the wafer, as shown, the CPW lines are brought into pressure contact with the circuits on the wafer. To define the contact area precisely, small fingers of relatively hard metal (i.e., nickel) are deposited on the gold CPW pattern at the probe tip. The nickel also has a much longer probe life than gold. Probes are generally categorized by their pitch, which is the center-to-center spacing between adjacent fingers. In this example, the fingers are labeled G-S-G which denotes a ground-signal-ground transmission line layout.

At frequencies below 65 GHz a coax to CPW transition has normally been used [1]. A waveguide to CPW transition was required to extend the upper frequency limit of wafer probes to 75 GHz, since commercially available coaxial cable assemblies overmode above 65 GHz. For a transition to be successful, two important conditions must be satisfied. First, the proper impedance transformation must take place and second, that the electric field patterns are properly matched at the input and output. In this case, the transformation is from a *V*-band rectangular waveguide, having a characteristic impedance [2] ranging from 400 to 520 Ω (versus frequency) and a TE_{10} electric field pattern, to a coplanar waveguide of 50 Ω and an electric field which is planar and opposed.

Manuscript received March 26, 1991; revised August 1, 1991. This work sponsored by Ball Aerospace under the Navy MMIC Phase III contract.

The author is with Cascade Microtech, 14255 S. W. Brigadoon Ct., Beaverton, OR 97005.

IEEE Log Number 9103291.

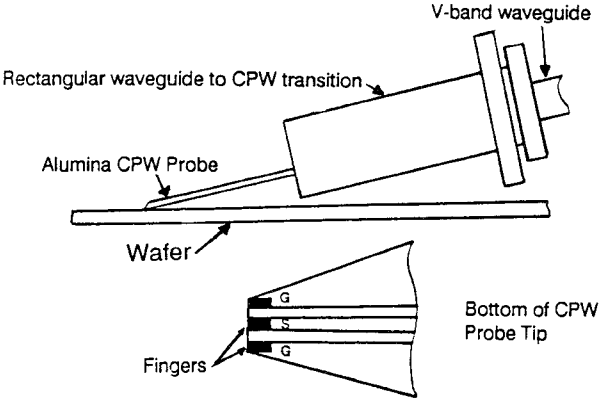

Fig. 1. Operational diagram of the *V*-band wafer probe.

The basic electric field transition steps are shown in Fig. 2 starting with the rectangular waveguide TE_{10} field pattern as shown in (a). The first step is to introduce a ridge into the waveguide which sets up a quasi-TEM field distribution (b). Next, a trough is introduced in the waveguide floor and the ridge is gradually extended into close proximity of this trough as shown in (c). This extension of the ridge has the effect of splitting and rotating the TEM field to a field pattern very similar to that found in coplanar waveguide (d). The coplanar waveguide is inverted to allow the CPW grounds to join the waveguide lower wall and the signal line is connected to the ridge (e).

This concept of creating coplanar-like fields with a ridge in a trough is believed to be new, although similar field patterns have been achieved with a rectangular conductor in a slot [3], and with a ridge joining a printed circuit board with a center conductor in a slot, thus forming a CPW structure [4]. All three of these structures have the inherent advantage of splitting the electric field equally in magnitude and phase, although in the latter two an odd mode may be excited between the slot side walls, since there is no transverse conductor across the slot to maintain an equal potential as energy propagates along the structure. The trough performs this odd-mode suppression in the ridge-trough waveguide.

To design the transition from rectangular waveguide to this new ridge-trough waveguide structure a mathematical model had to be developed to compute the characteristic

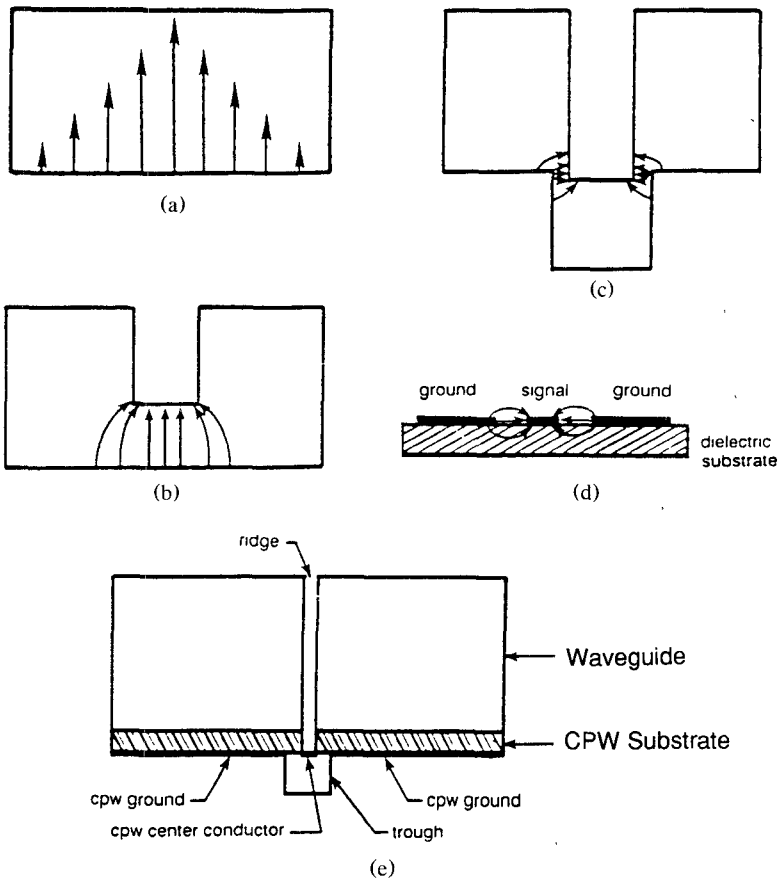

Fig. 2. Transition from TE_{10} electric fields to coplanar waveguide type fields. (a) TE_{10} mode within waveguide. (b) Ridge is introduced into waveguide. (c) Trough is introduced into waveguide. (d) Coplanar waveguide and associated fields. (e) Coplanar to ridge-trough waveguide joining.

impedance of the many transformer sections required to achieve a low VSWR. The need for a mathematical model was noted in [3] where it was stated that the impedance of the ridge in a slot structure was not calculated due to a lack of an appropriate formula.

The model developed was based primarily on research done by Cohn [5], Hopfer [6], and Chen [7] on modeling ridge waveguide. The details of the ridge-trough waveguide model will be presented in Section II.

A 25X scale model with variable ridge and trough dimensions was constructed concurrently with the development of the mathematical model to experimentally investigate this structure. Finding acceptable agreement between the mathematical model and the scale model, a complex transition was designed from a 50 Ω ridge-trough waveguide to conventional ridge waveguide. From the ridge waveguide standard techniques were used to transition to rectangular waveguide [6]. The results of the 25X model are presented in detail in Section III.

An actual *V*-band wafer probe was built after obtaining successful results for the whole transition from ridge-trough waveguide to rectangular waveguide in 25X model form. The probe could be biased with a dc voltage to allow testing of active devices. Important parameters such as the insertion loss and return loss of the probe were measured. The performance of the probe was better than required for successful probing of devices at *V*-band. These results are presented in Section IV.

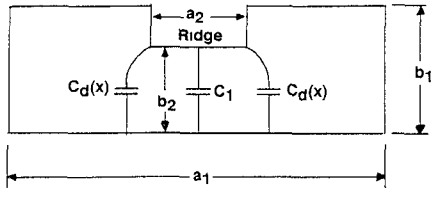

Fig. 3. Cross section of a ridge waveguide showing the capacitance due to both the parallel plate structure (C_1) and the discontinuity at the ridge corners ($C_d(x)$).

In Section V, the data obtained using a pair of *V*-band probes to make two port measurements of a FET is presented. Conclusions and suggestion for further work are found in Section VI.

II. A Mathematical Model for Ridge-Trough Waveguide

The standard single ridge waveguide, Fig. 3, is considered first. The structure is comprised of a rectangular waveguide with a ridge attached to the upper waveguide wall as shown.

Two important design parameters of waveguides are cutoff frequency f_c and characteristic impedance Z_0. For

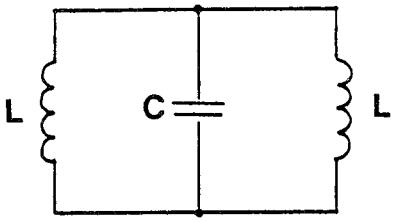

Fig. 4. Parallel LC circuit model used for determining the cutoff frequency of the ridge and ridge-trough waveguide structures.

determining the cutoff frequency, the electrical characteristics per unit length of both ridge waveguides and ridge-trough waveguides can be modeled by the circuit shown in Fig. 4. Each inductor L models the inductance from the longitudinal center of the ridge to the portion of the waveguide directly opposite the ridge. The two inductors represent the two alternate paths through which current can flow. A capacitor C models the capacitance between the ridge the rest of the waveguide.

Cutoff Frequency f_c

The fundamental mode cutoff frequency f_c is the resonant frequency of the parallel LC circuit of Fig. 4, thus

$$f_c = \frac{\omega_c}{2\pi} = \frac{1}{2\pi\sqrt{\frac{L}{2}C}} \tag{1}$$

The inductance and capacitance values, using the notation in Fig. 3, are given by

$$L = \frac{\mu(a_1 - a_2)}{2}(b_1) \tag{2}$$

$$C = \frac{\epsilon a_2}{b_2} + 2C_d(x). \tag{3}$$

The first term on the right side of (3) represents the electrostatic, parallel-plate capacitance between the waveguide's ridge and floor, while $C_d(x)$ represents the discontinuity capacitance present at the bottom corners of the ridge. As described by Chen [7] this discontinuity capacitance can be closely approximated by one of the fringing capacitance formulas developed by Whinnery and Jamieson [8]. Referring to the stepped waveguide geometry shown in Fig. 3, the formula for $C_d(x)$ is

$$C_d(x) = \frac{\epsilon}{\pi}\left[\frac{x^2+1}{x}\cosh^{-1}\left(\frac{1+x^2}{1-x^2}\right) - 2\ln\left(\frac{4x}{1-x^2}\right)\right] \tag{4}$$

where x equals the ratio b_2/b_1.

A similar analysis yields useable results for a ridge-trough waveguide; two cases are shown in Figs. 5 and 6. In the first case the ridge is wider than the trough, while in the second case the ridge is narrower and extends below the lower waveguide floor.

The ridge-trough waveguide is assumed to have the same inductance L as a ridge waveguide. Thus, the inductances of the ridge-trough waveguide configurations shown in Figs. 5 and 6 can be modeled by (2).

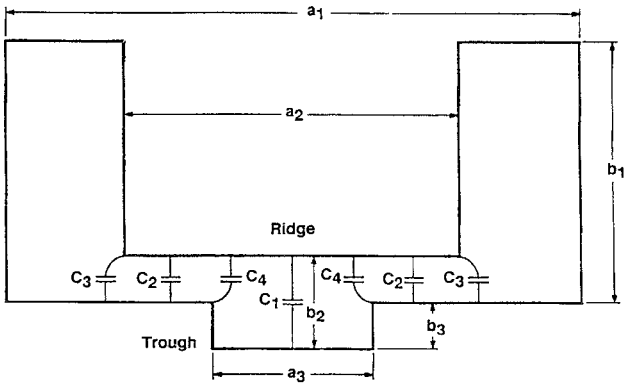

Fig. 5. Ridge-trough waveguide cross section for the case of a ridge wider than the trough.

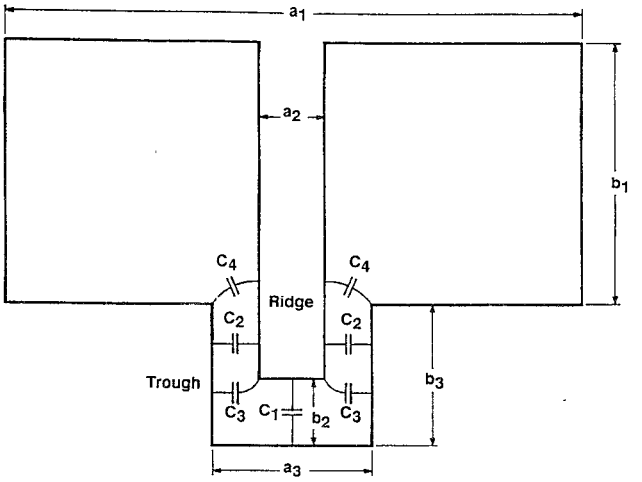

Fig. 6. Ridge-trough waveguide cross section for the case of a ridge narrower than and in the trough.

Compared to a ridge waveguide, a ridge-trough waveguide has a more complex cross section. The capacitance C of (1) for the ridge-trough waveguides shown in Figs. 5 and 6 is given by

$$C = C_1 + 2(C_2 + C_3 + C_4) \tag{5}$$

Capacitance C_1 is the electrostatic capacitance between the ridge and the center of the trough and can be modeled by

$$C_1 = \epsilon\frac{a_3}{b_2} \quad (6) \quad \text{and} \quad C_1 = \epsilon\frac{a_2}{b_2} \tag{7}$$

for Figs. 5 and 6, respectively.

Capacitance C_2 represents the additional electrostatic capacitance between the ridge and the floor of the ridge-trough waveguide shown in Fig. 5, or between the ridge and the sides of the trough of the ridge-trough waveguide shown in Fig. 6. Thus, C_2 can be modeled by

$$C_2 = \epsilon\frac{a_2 - a_3}{2(b_2 - b_3)} \quad (8) \quad \text{and} \quad C_2 = \epsilon\frac{2(b_3 - b_2)}{a_3 - a_2} \tag{9}$$

for Figs. 5 and 6, respectively.

Capacitance C_3 represents the fringing capacitance from the bottom corners of the ridge

$$C_3 = Cd(x) \tag{10}$$

where $C_d(x)$ is the function given in (4), and where x is the ratio $(b_2 - b_3)/b_1$ and the ratio $(a_3 - a_2)/2a_3$ for Figs. 5 and 6, respectively. Although the Whinnery and Jamieson model does not exactly agree with the configuration of Fig. 6, since the ridge does not contact either side of the trough, for the purposes of this model, the proximity of the ridge to the trough relative to the ridge's width a_2 lessens any errors this assumption introduces.

Capacitance C_4 represents the fringing capacitance between the upper corners of the trough and the ridge. Thus,

$$C_4 = Cd(x) \tag{11}$$

where x is the ratio $(b_2 - b_3)/b_2$ and the ratio $(a_3 - a_2)/(a_1 - a_2)$ for Figs. 5 and 6, respectively.

Characteristic Impedance Z_o

A ridge or ridge-trough waveguide's characteristic impedance can be found by determining the voltage-to-current ratio as described in Chen, cited above. The characteristic impedance Z_0 is

$$Z_o = \frac{V_o}{(I_{Z1} + I_{Z2})} = \frac{Z_{oi}}{\sqrt{1 - \left(\frac{f_c}{f}\right)^2}} \tag{12}$$

where I_{z1} and I_{z2} are two components of the current. Current I_{z1} is the longitudinal current component on the top and bottom plates which excites the waveguide's principal fields, while I_{z2} is the current component which produces local fields at the waveguide height changes.

A ridge waveguide's characteristic impedance at infinite frequency Z_{oi} is shown by Chen to be

$$Z_{oi} = \frac{120\pi}{2\frac{C_d(x)}{\epsilon}\cos\theta_2 + \frac{1}{\pi}\frac{\lambda_c}{b_2}\left(\sin\theta_2 + \frac{b_2}{b_1}\cos\theta_2 \tan\frac{\theta_1}{2}\right)} \tag{13}$$

where $\lambda_c = c/f_c$ is the wavelength of the signal at the cutoff frequency. The concept of impedance at infinite frequency is used to eliminate any dispersive effects at finite frequencies caused by the cutoff frequency of the waveguide structure. This results in the propagating wave being TEM in nature. The dispersive effects will be addressed later.

Using a similar analysis, detailed in Appendix I, the characteristic impedance at infinite frequency Z_{oi} for a ridge-trough waveguide as shown in Fig. 5 is

$$Z_{oi} = \frac{120\pi}{\frac{\lambda_c}{b_2\pi}\left\{\sin\theta_3 + \frac{b_2\cos\theta_3}{\sin(\theta_1+\theta_2)}\left[\cos\theta_1\left(\frac{1}{b_2-b_3} - \frac{1}{b_1}\right) - \frac{\cos(\theta_1+\theta_2)}{b_2-b_3} + \frac{1}{b_1}\right]\right\} + 2\cos\frac{\theta_3}{\epsilon}\left(C_4 + \frac{C_3\sin\theta_1}{\sin(\theta_1+\theta_2)}\right)} \tag{14}$$

where θ_1, θ_2 and θ_3 represent the phase angle in the voltage across the waveguide, starting with a maximum at the center of the ridge and decreasing to zero at the side wall. Angle θ_1 is the phase angle change in the horizontal distance between the waveguide's side wall and the edge of the center ridge,

$$\theta_1 = \frac{\pi(a_1 - a_2)}{\lambda_c}. \tag{15}$$

Angle θ_2 is the phase angle change on the horizontal distance between the edge of the ridge and the edge of the trough,

$$\theta_2 = \frac{\pi(a_2 - a_3)}{\lambda_c}. \tag{16}$$

Angle θ_3 is the phase angle change in the horizontal distance between the edge of the trough and the center of the trough,

$$\theta_3 = \frac{\pi a_3}{\lambda_c}. \tag{17}$$

Repeating the analysis for the waveguide configuration shown in Fig. 6 yields a Z_{oi} of

$$Z_{oi} = \frac{120\pi}{\frac{\sin\theta_3}{b_2} + \frac{\cos\theta_3}{\sin(\theta_1+\theta_2)}\left[\left(\frac{2}{a_3-a_2} - \frac{1}{b_1}\right)\cos\theta_1 - \frac{2\cos(\theta_1+\theta_2)}{a_3-a_2} + \frac{1}{b_1}\right] + \frac{2\cos\theta_3}{\epsilon}\left[C_3 + C_4\frac{\sin\theta_1}{\sin(\theta_1+\theta_2)}\right]}. \tag{18}$$

Angle θ_1 is the phase angle change within the horizontal distance between the waveguide's side wall and the edge of the center ridge, and is the same as defined in (15) above. Angle θ_2 is the phase angle change within the vertical distance where the width overlaps the edge of the trough, thus

$$\theta_2 = \frac{2\pi(b_3 - b_2)}{\lambda_c}. \tag{19}$$

Angle θ_3 is the phase angle change within the horizontal distance between the edge of the ridge and the center

of the ridge, thus

$$\theta_3 = \frac{\pi a_2}{\lambda_c}. \tag{20}$$

Once the characteristic impedance at infinite frequency Z_{oi} has been determined, the characteristic impedance Z_o at a finite frequency, f, may be calculated. By using the relation for wave propagation in a structure with a cutoff frequency, f_c:

$$Z_o = \frac{Z_{oi}}{\sqrt{1-\left(\frac{f_c}{f}\right)^2}}. \tag{21}$$

Model Results

Using the characteristic impedance equations presented above the impedance of a ridge-trough waveguide can be calculated as a function of ridge and trough dimensions. Nomographs such as shown in Fig. 7 were generated, in which the lines are traces of the path that the lower corners of a ridge would follow to maintain the indicated impedance. Constant impedance contour lines are shown for 30, 50, and 70 Ω. For example, if ridge "A" touches at points 1′ and 1 and ridge "B" touches at points 2′ and 2, both ridges will have the same impedance of 50 Ω, although their electric field distributions will be different. In the next section the results of the 25X model will be presented and compared to these predicted results.

Because the above equations assumed the ridge is either wider then the trough, or extends into the trough, the contour lines in Fig. 7 are estimated for those locations where the ridge is narrower than the trough, yet does not extend within the trough. It will be apparent that alternative means for determining the characteristic impedance of a ridge-trough waveguide, such as finite element analysis can be advantageously used for these and other ridge-trough waveguide configurations.

III. 25X Model Results

Ridge-Trough Model

A model of the ridge-trough structure was constructed at a scale 25 times larger than to be used at *V*-band to study the ridge-trough structure in detail. The 25X scaling factor was selected for two reasons. First it was anticipated that tolerances of finer than .001 inch would be required in the actual *V*-band probe. At 25X this scales to .025 inch which is a tolerance that could easily be held, at a reasonable price, during the machining of the numerous parts required for the model. A second consideration is that the 50 to 75 GHz frequency range is now scaled down to 2 to 3 GHz which makes the process of interfacing between the Hewlett-Packard 8510 network analyzer and the scale model a much easier task, due to these relatively low frequencies.

The basic measurement scheme is shown in Fig. 8. The HP 8510 is connected to a 25X coplanar waveguide board

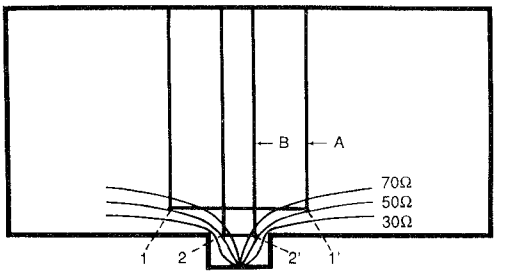

Fig. 7. Ridge-trough waveguide impedance nomograph for 30, 50, and 70 Ω. Two 50 Ω ridges, A and B, are shown.

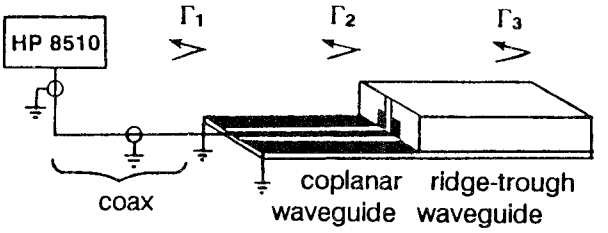

Fig. 8. Test line for investigating various ridge-trough waveguide dimensions for minimum return loss (Γ_2) at the coplanar waveguide to ridge-trough waveguide interface.

via a coax cable. The coplanar waveguide was fabricated by bonding copper foil to a .250 inch stycast substrate having a dielectric constant of 10. The dimensions of the foil were selected for 50 Ω characteristic impedance. This simulates the coplanar probe board in the *V*-band probe. The other end of the coplanar waveguide board is butted up against the 25X ridge-trough waveguide structure. It is at this interface that the reflection coefficient (Γ_2) will be minimized when an optimal match has been achieved. Additional reflection coefficients are caused by the coax-to-coplanar waveguide transition (Γ_1) and the open end of the ridge trough waveguide (Γ_3).

A large selection of ridge and trough dimensions were investigated. To help limit the number of permutations the ridge width was held in the .200 to .300 inch range, since the coplanar waveguide signal line width scales to .250 inch. Similarly the trough width was held to values close to .450 inch, since this is the separation of the two ground planes on either side of the signal line. Both the ridge and trough positions were adjustable along the vertical axis. The ridge-trough dimensions were held constant along the three foot length of the model.

Time domain reflection (TDR) and frequency domain data, such as that shown in Fig. 9, were taken for each set of dimensions. In this graph the lower trace is the TDR information showing the three reflection coefficients (Γ_1, Γ_2 and Γ_3). For this example the reflection coefficient at the interface (Γ_2) is observed to be less than 0.05. The upper trace is a return loss versus frequency plot of the Γ_2 region only, which was selected with the gating function of the HP 8510. Return loss is observed to be better than 22 dB for 2–3 GHz, which corresponds to 50–75 GHz, due to the 25X scaling factor.

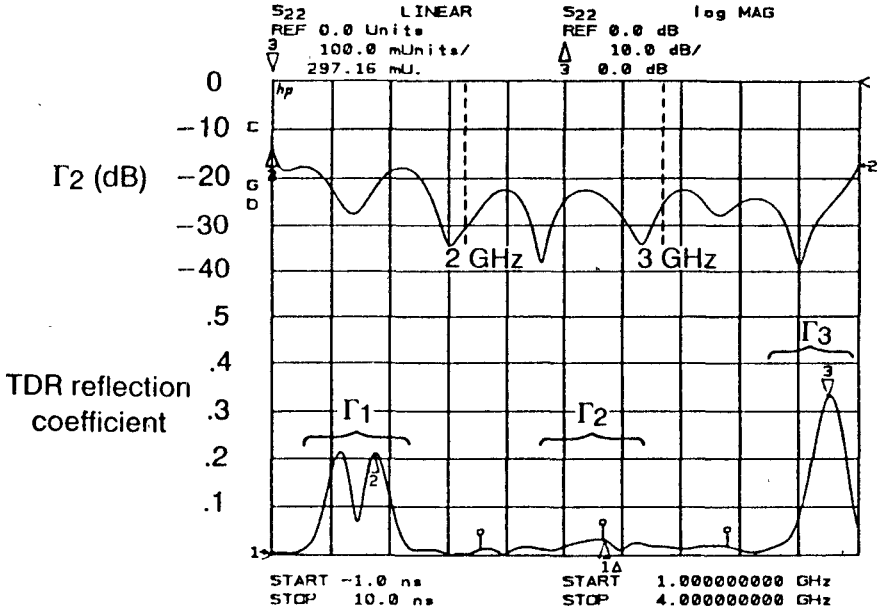

Fig. 9. TDR results for a coplanar waveguide to ridge-trough waveguide transition. The reflection at the interface is denoted as Γ_2. The return loss Γ_2 versus frequency (1–4 GHz) is shown at the top.

Next the dimensions for ridge-trough structures giving better than 20 dB return loss for Γ_2 were plotted on nomographs similar to Fig. 7. It was found that the mathematical model predicted values of characteristic impedances slightly higher than 50 Ω for these ridge and trough dimensions, typically between 55 to 65 Ω. One possible implication is that due to limitations of the mathematical model the calculated values are about 20 percent higher than is actually the case. A second possibility is that the 25X transmission line is higher than 50 Ω. Using a model described by Gupta [9], the theoretical impedance of the 25X coplanar line was computed to be 53 ± 1. If an impedance of 53 Ω is assumed then the ridge-trough mathematical model appears to predict impedances that are 2 to 12 Ω higher than experimental data suggests is the actual value. This accuracy was felt to be adequate for the design of the transition.

Transition Model

A transition was next designed using the mathematical model. The function of this transition was to convert the coplanar electric fields present in the ridge-trough waveguide to the TEM like fields characteristic of ridge waveguide, as shown in Fig. 2. This was accomplished by using the five quarter-wavelength sections as shown in Fig. 10. Each section was designed to have a characteristic impedance of 50 Ω.

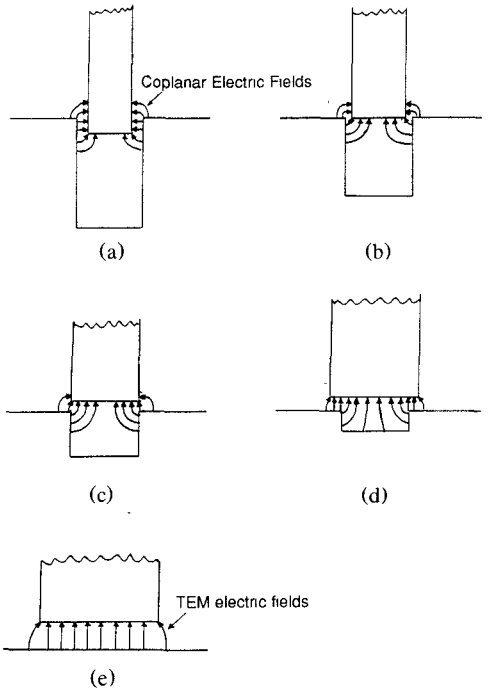

Fig. 10. Five different waveguide sections, all 50 Ω characteristic impedance, used to transition from coplanar to TEM electric field patterns. (a) Ridge in trough. (b) Ridge even with trough. (c) Ridge over trough. (d) Ridge overlapping trough. (e) Conventional ridged waveguide, no trough.

Although section (e) is both 50 Ω and ridge waveguide, the ridge itself is relatively narrow (0.19 of the waveguide width) compared to normal ridge waveguide. For this reason one more 50 Ω section was added that was slightly wider to give a ridge to waveguide width ratio of 0.26. Following this intermediate 50 Ω section is a seven section binomial (i.e., maximally flat) transformer to transition from the ridge-waveguide to the rectangular waveguide output. The binomial transformer was selected instead of a cosine or exponential taper, since the quarter-wavelength sections were preferable from a machining stand point due to assembly constraints.

The next step was to fabricate the entire transition in a 25X model. The results are shown in Fig. 11 and were obtained using the test line described in Fig. 8. The return loss for the entire transition from the ridge-trough

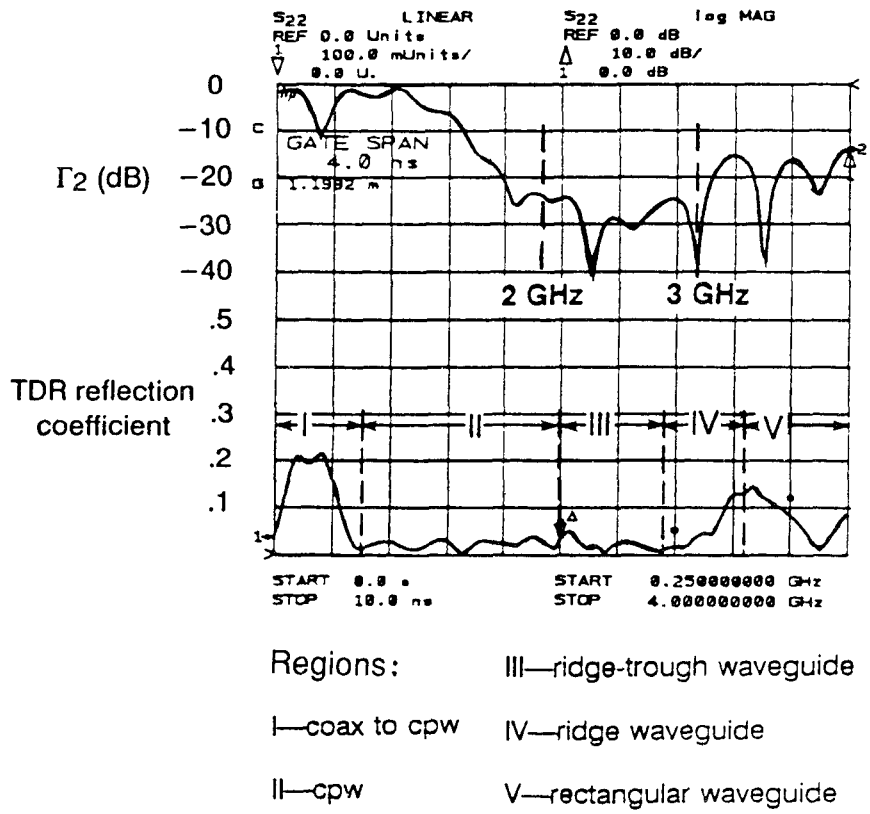

Fig. 11. TDR and S_{11} data for a 25X coplanar to rectangular waveguide transition.

input to the rectangular waveguide output is shown. A worst case of 23 dB return loss is observed across the 2 to 3 GHz band, which seems reasonable considering the significant electromagnetic field pattern changes occurring along this complex transition. The return loss goes to zero at the low end of the band due to the 1.4 GHz cutoff frequency of the 4.3 inch wide rectangular waveguide output. This is also observed as large bump in the TDR plot in regions IV and V. The bump decreases towards the end of region V due to radiation out the open end of the waveguide. A resonance is present at about 0.3 GHz due to the 36 inch long model supporting a half wavelength mode at this frequency. The bandpass characteristics of the binomial transformer are observed as an increase in the reflection coefficient above 3 GHz.

IV. Construction Techniques and Test Results for the V-Band Wafer Probe

Construction Techniques

The construction techniques employed are illustrated in Fig. 12. The probe block is split into upper and lower halves as shown. An insulating layer is placed between the two halves to provide dc isolation. Quarter wavelength RF chokes generate a virtual ground where the waveguide interior surface is split to minimize RF losses.

The alumina probe board is captured in a pocket which is machined into the upper block. The probe board is oriented such that the metalized ground-signal-ground lines are facing down, since this is the surface that must

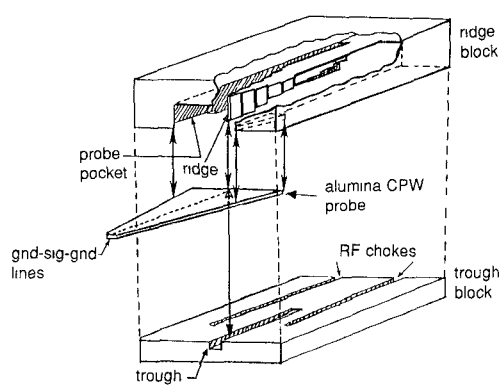

Fig. 12. Exploded view of the V-band probe.

contact the wafer. A bond ribbon joins the signal line (shown by a dashed line) to the ridge after the probe has been situated in the upper block. When the lower block is joined to the upper block the probe board is clamped into place. This clamping action also brings the ground metalization of the probe board into electrical contact with the lower block. The end result is that the signal line and ground lines are electrically isolated and may be biased by applying a voltage to the upper and lower block halves respectively. In the event of probe board breakage the two halves may be separated and a new probe board installed.

If a waveguide was attached to the rear of this structure, at the rectangular waveguide input port, it would short the upper and lower blocks together preventing

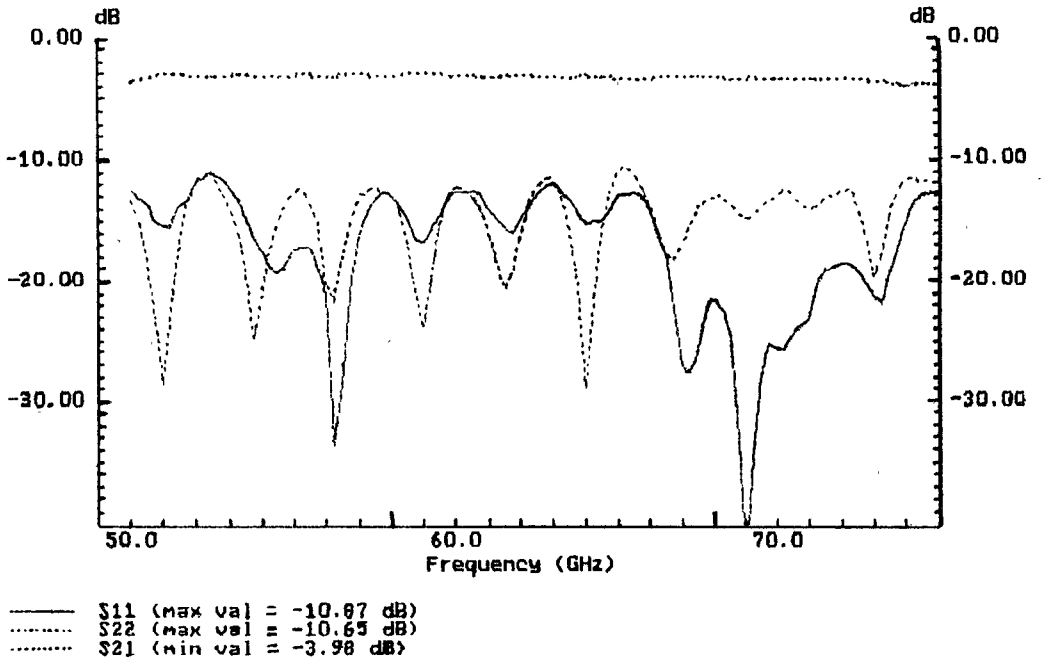

Fig. 13. Insertion loss and return loss for a 100 μ pitch probe. Port 1 is the rectangular waveguide input and port 2 is the probe board tip.

biasing of the probe. For this reason a third block is located at the rear of the probe which is dc isolated from the upper block to allow biasing. This rear block then provides a mounting surface for the V-band waveguide used for connecting to the test equipment.

Test Results

Tests were performed to characterize the V-band probe. The method used is as follows: First a calibration is performed at the waveguide flange that is to be attached to the V-band probe waveguide input port. Waveguide standards for V-band waveguide were used. This process establishes a reference plane at the probe input port. Next the waveguide is attached to the probe input port and a second calibration is performed at the tip of the alumina probe tip. A Cascade Microtech Inc. LRM Impedance Standard Substrate (ISS) was used for this calibration. Standards such as 50 Ω loads, short circuits, and 50 Ω transmission lines are found on this ISS. By measuring the S11 for a match (50 Ω), short, and open the probe may be characterized [10] using a standard de-embedding routine.

The results for a V-band probe having a 150 μ pitch are shown in Fig. 13. The insertion loss is better than 4 dB across the 50 to 75 GHz band. Two reflection coefficients are shown: S_{11} and S_{22}, which are the reflection coefficients at the rectangular waveguide input port and at the tip of the alumina probe board, respectively. For this probe the worst case values (i.e., maximum) were 10.9 dB for S_{11} and 10.7 dB for S_{22}.

It has been experimentally determined that if $|S_{11}|-|S_{21}| > 5$ dB, the HP 8510 Network Analyzer can correct the measured data to obtain accurate characterization of the device under test. It is clear that this V-band probe exceeds this minimum performance goal.

V. Data Obtained at V-Band with a Pair of V-Band Wafer Probes

A pair of V-band probes were constructed to allow two port measurements at V-band. Fig. 14 shows the two probes mounted on a Cascade Microtech Inc. Summit 9000 probing station. Two flexible waveguide cables, visible at the rear, have about 3 dB insertion loss in the 50–75 GHz band. A bias cable is attached to the side of each probe to allow testing of active devices.

A pseudomorphic MODFET with a 0.25 μ gate width was tested. The S_{21} data for this device is shown in Fig. 15. The device has $S_{21} = 1$ at 58.5 GHz. Passive devices such as capacitively coupled filters have also been characterized, even when their insertion loss exceeded 30 dB.

VI. Conclusion

Under the Navy Phase III MMIC program a waveguide input wafer probe was successfully developed that covers the 50 to 75 GHz frequency range. The probe is biasable and has the provision for replacing probe boards should they become worn or broken. The probe has been demonstrated to work successfully by measuring both active and passive devices.

During the course of the V-band probe development a new type of waveguide structure was developed and characterized: the ridge-trough waveguide. This waveguide has a coplanar-like electric field distribution and much broader fundamental mode bandwidth than normal rect-

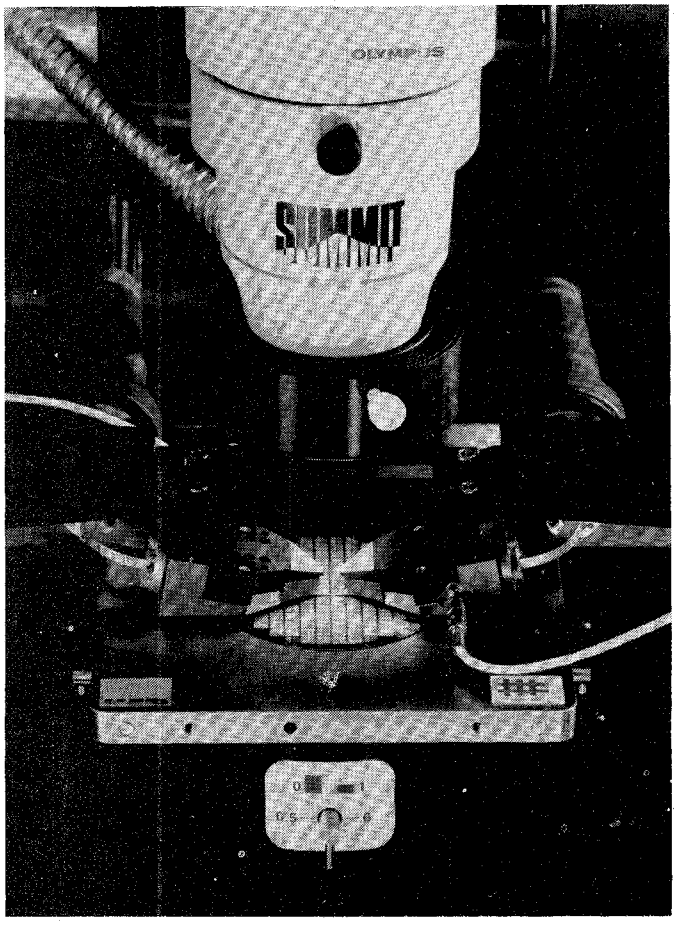

Fig. 14. V-band probe station for two port measurements. Note the rectangular waveguide bends bolted to the probe ends and bias cables plugged into the sides.

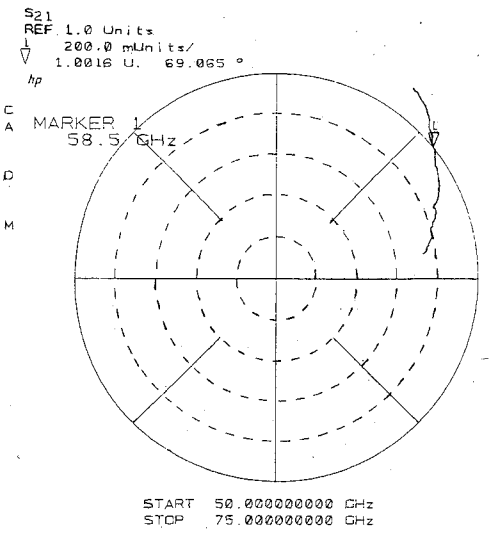

Fig. 15. S_{21} polar plot for a MODFET.

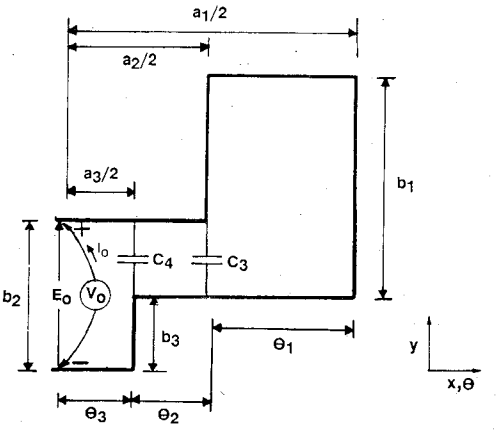

Fig. 16. Half-circuit model of the ridge-trough waveguide used for derivation of the impedance at infinite frequency. A voltage source V_o is applied across the ridge and trough generating an electric field E_o.

angular waveguide. A mathematical model of the ridge-trough waveguide was also developed allowing a complex transition to be developed. This transition performed the necessary conversion of the 50 Ω ridge-trough waveguide to the standard V-band waveguide output.

25X models were constructed to characterize the ridge-trough waveguide and test the complex transition mentioned above. These models allowed verification of the results predicted by the mathematical model. Good agreement was found, although further improvement could probably be achieved with a finite element model.

A pair of probes were constructed, which allowed a MODFET to be measured.

VII. Appendix

A derivation for the characteristic impedance at infinite frequency for the structure shown in Fig. 5 is presented. By assuming the frequency to be much greater than the cutoff frequency (i.e., "infinite") the wave propagation down the waveguide may be assumed to be TEM in nature.

The characteristic impedance is found by solving for the total current, I_o, produced when a test voltage, V_o, is applied across the ridge and trough surfaces as shown in Fig. 16. This relation is expressed as

$$Z_o = \frac{V_o}{I_o} = \frac{V_o}{I_{z1} + I_{z2}}. \tag{22}$$

The total current being comprised of two basic components: the longitudinal current I_{z1} on the top and bottom plates generates the waveguide's principle fields, and I_{z2} the current which produces local fields at the waveguide height changes. The z subscript refers to the z axis which is normal to the x and y axis shown in Fig. 16.

The analysis will be divided into three sections. First the longitudinal current, I_{z1}, is solved for as a function of electric field E_y. Next the current I_{z2} is solved for in terms of the voltage at the discontinuity. Finally the electric field and voltage, as a function of position in the waveguide, are solved for. This allows a solution for the characteristic impedance at infinite frequency as a function of the waveguide dimensions.

Longitudinal Current I_{z1}

The longitudinal current I_{z1} in the top and bottom waveguide surfaces can be expressed in terms of the incremental sheet current $i(x)$:

$$I_{z1} = 2\begin{vmatrix} a_3^-/2 & a_2^-/2 & a_1/2 \\ \int i(x)\,dx + & \int i(x)\,dx + & \int i(x)\,dx \\ 0 & a_3^+/2 & a_2^-/2 \end{vmatrix}, \quad (23)$$

where the $-$ and $+$ indicate that the integral is evaluated to either the left or right side of the waveguide height discontinuity. Since these integrals are for a half circuit only, the multiplication factor of two is required for the total current.

Using Ampere's law the following result is obtained:

$$i(x)\,dx = \oint \boldsymbol{H}\cdot d\boldsymbol{l} = H_x(x)\,dx. \quad (24)$$

Further reduction is obtained by using the relation $H_x(x) = E_y(x)/120\pi$ in (24). Substitution into (23) yields

$$I_{z1} = \frac{2}{120\pi}\begin{vmatrix} a_3^-/2 & a_2^-/2 & a_1/2 \\ \int E_y(x)\,dx + & \int E_y(x)\,dx + & \int E_y(x)\,dx \\ 0 & a_3^+/2 & a_2^+/2 \end{vmatrix}. \quad (25)$$

For convenience in later analysis the integrals can be evaluated over electrical phase length θ instead of physical length x. The relation used is: $(\lambda_c/2\pi)\,d\theta = dx$, where λ_c is the cutoff wavelength. This substitution yields

$$I_{z1} = \frac{\lambda_c}{120\pi^2}\begin{bmatrix} \theta_3^- & (\theta_2+\theta_3)^- & \theta_1+\theta_2+\theta_3 \\ \int E_y(\theta)\,d\theta + & \int E_y(\theta)\,d\theta + & \int E_y(\theta)\,d\theta \\ 0 & \theta_3 + & (\theta_2+\theta_3)^+ \end{bmatrix}. \quad (26)$$

Discontinuity Current I_{z2}

In Chen [7] a derivation is given for the current associated with a height change discontinuity in the waveguide. It is briefly outlined here. For a height change at a location θ there is local electric field produced over some width W. A total charge Q will also be present in this region. Using Gauss' law

$$(\epsilon E)(W)(1) = Q = C_d V(\theta), \quad (27)$$

where E is the electric field intensity and $V(\theta)$ is the voltage at the discontinuity. This is rearranged to give

$$E = \frac{C_d V(\theta)}{\epsilon W}.$$

Linked to the electric field, E, is the magnetic field, H. These quantities are related by $H = E/120\pi$. Using Ampere's law yields a solution for the current at the discontinuity

$$I_{z2}(\theta) = 2HW = \frac{2C_d V(\theta)}{\epsilon 120\pi}. \quad (28)$$

For the structure in Fig. 6 the total current due to height changes is

$$I_{z2} = \frac{2C_4 V(\theta_3)}{\epsilon 120\pi} + \frac{2C_3 V(\theta_2+\theta_3)}{\epsilon 120\pi}, \quad (29)$$

where C_3 and C_4 are given by (10) and (11).

Electric Field

If it is assumed that only the TE_{10} mode is propagating in the waveguide the electric field distribution is constant with frequency [5]. This implies that the electric field distribution at infinite frequency is the same as at cutoff. For the structure shown in Fig. 16 the boundary conditions were solved to yield the following electric field and voltage solutions:

Electrical Location	Electric Field Intensity $E_y(\theta)$	Voltage $V(\theta)$
$\theta = 0$		$V_o = E_o b_1$
$0 < \theta < \theta_3$	$E_y(\theta) = E_o \cos\theta$	
θ_3		$V(\theta_3) = E_o b_3 \cos\theta_3$
$\theta_3 < \theta < \theta_2 + \theta_3$	$E_y(\theta) = E_o\left(\frac{b_2}{b_4}\right)\frac{\cos(\theta_3)\sin(\theta_1+\theta_2+\theta_3-\theta)}{\sin(\theta_1+\theta_2)}$	(where $b_4 = b_2 - b_3$)
$\theta_2 + \theta_3$		$V(\theta_2+\theta_3) = E_o b_3 \frac{\cos(\theta_3)\sin(\theta_1)}{\sin(\theta_{1+}\theta_2)}$
$\theta_2 + \theta_3 < \theta < \theta_1 + \theta_2 + \theta_3$	$E_y(\theta) = E_o\left(\frac{b_3}{b_1}\right)\frac{\cos(\theta_3)\sin(\theta_1+\theta_2+\theta_3-\theta)}{\sin(\theta_1+\theta_2)}$	
$\theta_1 + \theta_2 + \theta_3$		$V(\theta_1+\theta_2+\theta_3) = 0.$

When the above expressions for the electric fields and voltages are substituted into the expressions for I_{z1} and I_{z2}, respectively, (22) becomes (14).

Acknowledgment

Thanks to K. Jones, B. Duman, G. Benedict, R. Warner, D. DeLessert, D. d'Almeida, A. Davidson and S. Lauer for their contributions.

The MODFETs were supplied by Dr. M. Trippe of M. Marietta Labs, and G. Martin of Boeing Research Labs. F. Beckous of W. L. Gore & Associates, Inc. supplied flexible waveguide.

References

[1] K. E. Jones, E. W. Strid, and K. R. Gleason, "mm-Wave Wafer Probes Span 0 to 50 GHz," *Microwave J.*, Apr. 1987.
[2] R. E. Collin, *Foundations for Microwave Engineering*. New York: McGraw-Hill, 1966, pp. 99.
[3] G. C. Dalman, "New waveguide-to-coplanar waveguide transition for centimeter and millimeter wave applications," *Electronic Letters*, vol. 26, June, 1990, pp. 830–831.
[4] G. E. Ponchak and R. N. Simons, "A new rectangular waveguide to coplanar waveguide transition," in 1990 *IEEE MTT-S Int. Microwave Symp. Dig.*, vol. I, pp. 491–493.
[5] S. B. Cohn, "Properties of ridge waveguide," *Proc. IRE*, vol. 35, pp. 783–788, Aug. 1947.
[6] S. Hopfer, "The design of ridged waveguides," *IRE Trans. Microwave Theory Tech.*, vol. 3, pp. 20–29, Oct., 1955.
[7] T.-S. Chen, "Calculation of the parameters of ridge waveguides," *IRE Trans. Microwave Theory Tech.*, vol. 5, no. 1, pp. 12–17, Jan., 1957.
[8] J. R. Whinnery and H. W. Jamieson, "Equivalent circuits of discontinuities in transmission lines," *Proc. IRE*, vol. 32, pp. 98–116, Feb., 1944.
[9] K. C. Gupta, R. Garg, and I. J. Bahl, *Microstrip Lines and Slotlines*. Norwood MA: Artech House, 1979, pp. 275–280.
[10] D. E. Carlton, K. R. Gleason, and E. W. Strid, "Microwave wafer probing," *Microwave J.*, Jan. 1985.
[11] W. L. Gore & Associates: GORE-TEX Flexible Dielectric Waveguide, Type B.
[12] MODFETs supplied by Dr. Michael Trippe of Martin Marietta Labs.
[13] MODFETs supplied by Glenn Martin of Boeing Research Labs.

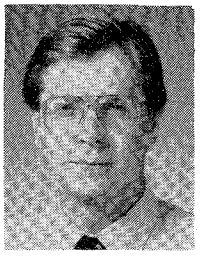

Edward M. Godshalk was born in Minocqua, WI on September 25, 1958. He received the B.S. and M.S. degrees in electrical engineering from Washington University, St. Louis, MO, in 1982 and 1983, respectively.

From 1983–1985, he worked for Central Microwave Company, where he developed *Ka* band MIC VCO's, Gunn diode reflection amplifiers, and ferrite devices. He was with Millitech Corporation from 1985–1989 and helped develop millimeter wave digital radios, cryogenic receivers, Gunn oscillators, and circulators. He joined Cascade Microtech in 1989, currently heads the Electrical Engineering group, and developed the waveguide input wafer probe.